Research Article | Vol. 31, No. 20 / 25 Sep 2023 / Optics Express 32543
Optics EXPRESS

Simultaneous measurement of temperature and salinity based on a hole-assisted dual-core fiber

YU LIU,[1] JING YANG,[1,4] YUXIAO XUE,[1] SHAN GAO,[1] PEIXUAN TIAN,[1] PENG YE,[1] ZHENYU DUAN,[1] JINHUI SHI,[1] JUN YANG,[1] LIBO YUAN,[2] K. T. V. GRATTAN,[3] AND CHUNYING GUAN[1,*]

[1]*Key Laboratory of In-Fiber Integrated Optics of Ministry of Education, College of Physics and Optoelectronic Engineering, Harbin Engineering University, Harbin 150001, China*
[2]*Photonics Research Center, Guilin University of Electronics Technology, Guilin 541004, China*
[3]*School of Science & Technology, City, University of London, Northampton Square, London, EC1V 0HB, UK*
[4]*yangjing13@hrbeu.edu.cn*
[*]*cyguan@163.com*

Abstract: An optical fiber sensor based on a hole-assisted dual-core fiber (HADCF) has been proposed and experimentally demonstrated for dual-parameter measurements. The dual-mode interferometer created uses the LP_{01} mode and LP_{11} mode in the suspended core of a specialist optical fiber, combined with a directional coupler formed by using the suspended core and the center core in a 16 mm long HADCF. Using this, the simultaneous measurement of salinity (due to the presence of NaCl) and temperature has been achieved through monitoring the interference dip and resonance dip. The sensitivities of the measurement of salinity and temperature are 190.7 pm/‰ and -188.2 pm/°C, respectively. The sensor developed has the advantages of simplicity of fabrication, a high level of integration and the potential for measurement of dual parameters, supporting its potential applications in marine environment measurements.

1. Introduction

Salinity (the concentration of NaCl) or saltiness can be used to indicate the movement of seawater and thus, for example, the distribution of marine creatures. It is thus a basic parameter for better information on the marine environment [1,2], with the measurement of salinity being an essential tool of marine science. Currently, commercial conductivity-temperature-depth (CTD) systems are widely used for marine environmental monitoring, this depending on the correspondence between chloride ion content and conductivity in seawater and used for the required salinity measurements [3]. However, this technology is affected by electromagnetic interference, a problem which leads to errors in the measurements made. In addition, CTD systems have the disadvantage of high maintenance costs, difficulties in long-distance transmission and long-term operation in severe environments [4]. Optical fiber sensors have attracted significant attention in the field of seawater monitoring, given their ability to overcome the disadvantages mentioned above of conventional technology. Optical fiber salinity sensors generally measure salinity by detecting the refractive index (RI) of seawater. Several different measurement methods in optical fiber salinity sensors have been proposed, including optical refraction [5], fiber gratings [6,7], fiber interferometers [8,9], and surface plasmon resonance (SPR) [10–12]. Although these salinity sensors all work on different principles, their sensitivities are affected by the intensity of the evanescent field which is monitored. The strong evanescent field that is present can amplify the interaction between the light and the seawater, to improve the sensitivities of the sensors to salinity. Thus, in order to enhance the strength of the evanescent field and optimize the sensing performance, a number of different types of optical fiber salinity sensors have been fabricated by using fiber

#500576 https://doi.org/10.1364/OE.500576
Journal © 2023 Received 14 Jul 2023; revised 3 Sep 2023; accepted 3 Sep 2023; published 14 Sep 2023

Optics EXPRESS

post-processing techniques, such as fiber tapering [13], side polishing [14] and cladding etching [15]. These operations applied to the optical fiber can improve the performance of the sensors, but a disadvantage is that they also disrupt the mechanical strength of the fiber, which then limits their use in different practical applications. To avoid affecting the mechanical properties of the optical fiber, two-dimensional materials are coated on the optical fiber, to increase the sensitivity of the sensor created [16–19]. The method used is helpful in improving the sensing performance, relying on the abundance of the hydrophilic functional groups (-O, -F, and-OH), the large specific surface, and the broad-spectrum absorption characteristics, which preserve the structural integrity of the optical fiber. Hernaez et al. have demonstrated a fiber-based ethanol sensor, coated with graphene oxide (GO), and based on lossy mode resonance (LMR) [19]. The sensors created using the GO coating have demonstrated a maximum sensitivity enhancement of 176% (with respect to not using the GO coating). Li et al. have proposed an ultra-sensitive optical fiber salinity sensor, based on 2D Ti_3CN MXene, where an ultra-high salinity sensitivity of -5.34 nm/‰ was obtained [20]. However, the durability of such a sensor remains a problem for coated sensors using this material, especially when applied in corrosive and severe seawater environments. Further, the coating process itself on two-dimensional materials is also a difficult problem.

Mach-Zehnder interferometers (MZIs) have been widely used in a wide range of sensing applications taking advantage of simple fabrication processes and their high sensitivity [21–25]. Many such high-sensitivity fiber salinity sensors, based on MZI technology, have been reported [8,26–28]. However, salinity measurements are affected to a significant extent by temperature changes, so it is particularly important to measure salinity and temperature simultaneously. Generally, temperature effects can be compensated by using additional reference temperature sensors [29,30], which then increases the size and mass of the sensor and additionally, the different measurement location of the temperature sensing and RI measurement elements potentially affects the experimental results obtained.

In this work, an optical fiber sensor based on HADCF was experimentally demonstrated, to realize the simultaneous measurement of temperature and salinity. To create it, a segment of HADCF was spliced between two single mode fibers (SMFs), but with an offset included. An MZI and a directional coupler fit together well to in a single HADCF. Using this device, a series of interference dips and a resonance coupling dip were obtained simultaneously, at different wavelengths. As the MZI and the directional coupler have different responses to temperature and salinity, this provides a basis for a practical dual-parameter sensor. The sensor described in this paper has a compact structure, shows high sensitivity and good repeatability, and thus has significant potential application for applications in the field of marine environmental monitoring.

2. Structure and principle of optical fiber sensor

The photograph of the cross-section of the HADCF used in this work is shown in Fig. 1(a). The HADCF comprises a silica cladding, a center core, a suspended core and a large air hole, where their diameters are 125 μm, 10 μm, 12 μm, and 35 μm, respectively. The air hole is located at the side of the center core. The suspended core used is suspended on the inner wall of the air hole, which is the closest location to the center core. The distance between the centers of the suspended core and the center core was 15 μm and the RI difference between the core and the cladding was 0.005. Due to the small distance between the center core and the suspended core, the fiber can be used as a directional coupler at the phase-matching wavelength. Figure 1(b) shows the calculated dispersion curves for different low-order modes in the center and suspended cores of the HADCF. It can be seen that the dispersion curves of the fundamental modes of the center core and the suspended core intersect at a wavelength of 1350 nm. The LP_{11} mode in the suspended core cuts off at ~1410 nm.

The schematic diagram of the structure of the sensor discussed in this work is shown in Fig. 2(a). The sensor is composed of a section of the HADCF and two SMFs. Both ends of the suspended

Optics EXPRESS

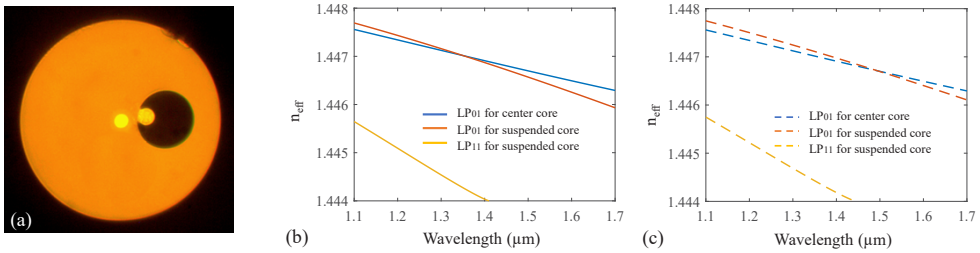

Fig. 1. (a) Photograph of the cross section of the HADCF. (b) and (c) The calculated dispersion curves for the low-order modes of the (b) air-filled and (c) water-filled HADCF.

core are fused to the SMFs with an appropriate offset, as shown in Fig. 2(b). Two micropores near the offset fusing points were fabricated by using femtosecond laser micromachining, to build a microfluidic channel, as shown in Fig. 2(c). The beam from the input SMF passes into the HADCF through the first offset fusing point, allowing the LP_{01} and LP_{11} modes in the suspended core to be excited simultaneously. At the second offset fusing point, the two modes were combined and coupled into the output SMF to form an MZI. The intensity of the interference in the MZI can be expressed as:

$$I = I_1 + I_2 + 2\sqrt{I_1 I_2}\cos(\Delta\varphi) \tag{1}$$

where I_1 and I_2 are the intensities of the light in the LP_{01} and LP_{11} modes in the suspended core. The phase difference between the LP_{01} and LP_{11} modes can be represented by:

$$\varphi = (2\pi\Delta n_{\text{eff}} L)/\lambda \tag{2}$$

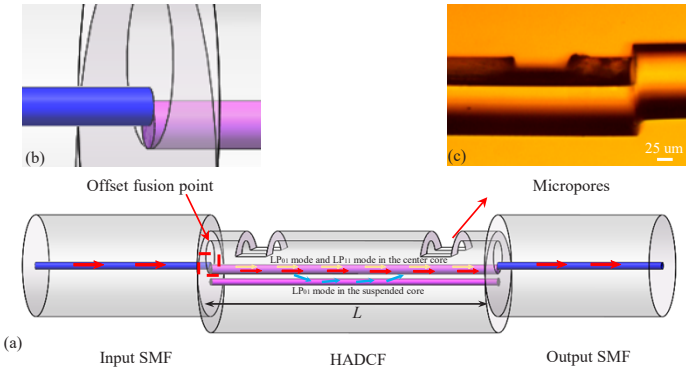

Fig. 2. (a) Schematic configuration of the sensor discussed in this work. (b) Enlarged lateral view near the offset point. (c) Micrograph of a micropore fabricated by using a femtosecond laser.

The free spectra range (FSR) can be expressed as shown below:

$$FSR = \lambda^2/(\Delta n_{\text{eff}} \cdot L) \tag{3}$$

where L is the length of the HADCF, and Δn_{eff} is the RI difference between the LP_{01} and LP_{11} modes. The relationship between the shift of the wavelength, λ, and the external RI, n_{ext}, can be

Optics EXPRESS

expressed as:

$$S = \frac{d\lambda}{dn_{ext}} = \lambda \cdot \frac{1}{\Gamma}\left(\frac{1}{\Delta n_{eff}}\frac{d\Delta n_{eff}}{dn_{ext}}\right) \tag{4}$$

where the dispersion factor $\Gamma<0$ in the wavelength range 1100 nm to 1500 nm, and as n_{ext} increases, the effective RI increases for both the LP_{01} and LP_{11} modes, but for the LP_{11} mode, this increases more rapidly, so that $d\Delta n_{eff} < 0$, and $d\Delta n_{eff}/d\Delta n_{ext} < 0$. Consequently, $S > 0$ when n_{ext} increases, the interference dips will show a red shift [31].

In order to achieve better interference visibility, the LP_{01} and LP_{11} modes in the suspended core need to be excited equally. With the different offsets, the excitation efficiencies of the LP_{01} and LP_{11} modes in the suspended core are different. The excitation coefficient used to describe the excitation efficiencies of the different modes is given below, as follows, where:

$$b = \frac{1}{4}\iint (\mathbf{E}_m \times \mathbf{H}_n{}^* + \mathbf{E}_n{}^* \times \mathbf{H}_m) \cdot \mathbf{z}\,dx\,dy \tag{5}$$

And where $\mathbf{E}_m$ and $\mathbf{H}_m$ are the normalized electric and magnetic fields of fundamental mode in the SMF, $\mathbf{E}_n$*and $\mathbf{H}_n{}^*$ are the complex conjugates of the normalized electric and magnetic fields of one mode in the suspended core of HADCF, and $\mathbf{z}$ is the unit vector along the propagation direction of the beam. The finite element method was used to calculate the electric and magnetic fields of the fundamental and LP_{11} modes in the suspended core of HADCF and the fundamental mode in the SMF. The excitation coefficient can be obtained by substituting the normalized electric and magnetic fields into Eq. (5). The excitation coefficients of the LP_{01} and LP_{11} modes in the suspended core (without liquid in the hole) and monitored at a wavelength of 1210 nm are shown in Fig. 3(a). At 1210 nm, the LP_{01} and LP_{11} modes exist simultaneously. With the increase of the offset, the excitation coefficient of the LP_{11} mode reaches a maximum at an offset of 3.65 μm, while that of the LP_{01} mode decreases monotonically. In order to obtain the maximum extinction ratio in the interference spectrum, the excitation coefficients of the LP_{01} and LP_{11} modes should be equal, and consequently the optimum offset was determined to be 4.2 μm. The optimum offset will be seen to change slightly when the hole is filled with solutions of different salinities, as shown in Fig. 3(b).

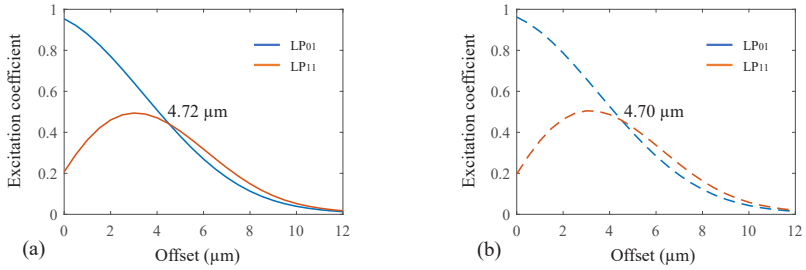

Fig. 3. Excitation coefficients of LP_{01} and LP_{11} modes in the suspension core for (a) air- and (b) saline solutions (n = 1.333)-filled HADCF.

Meanwhile, due to the small distance between the center core and the suspended core, the HADCF can be regarded as a directional coupler. Based on coupled-mode theory, the amplitudes of the optical fields in two cores can be represented by the following formulae:

$$\frac{dA_c(z)}{dz} = iK_{sc}A_s(z)e^{i(\beta_c-\beta_s)z} \tag{6}$$

$$\frac{dA_s(z)}{dz} = iK_{cs}A_c(z)e^{i(\beta_s-\beta_c)z} \tag{7}$$

Optics EXPRESS

where A_s, A_c, and β_s, β_c are the amplitudes and the propagation constants of the modes in the suspended and center cores, respectively. K_{cs} and K_{sc} are the coupling coefficients between the modes in the center and suspended cores. Resonance coupling occurs when the propagation constants of the two modes are equal or sufficiently close. The dispersion curves of the fundamental modes of the center and suspended cores intersect at a wavelength of 1350 nm, indicating that strong coupling can occur.

When the air hole is filled with liquid, the effective RI of the fundamental mode of the suspended core increases as the RI around the core becomes large. Meanwhile, the center core is not affected, so that the phase matching wavelength changes it redshifts. Figure 1(c) shows the calculated effective RIs for different low-order modes in the center and suspended cores of a water-filled HADCF. The results of a simulation of the beam propagation in the sensor using the beam propagation method is shown in Fig. 4. Figure 4(a) shows the profile structure scheme of the proposed sensor. At wavelengths of 1100 nm and 1111 nm, well away from the phase matching wavelength of 1350 nm, the LP_{01} and LP_{11} modes in the suspended core were excited simultaneously at the offset fusing point, as shown in Figs. 4(b), 4(c), 4(e) and 4(f), and are combined at the second offset fusion point and form an MZI. The center and suspended cores show phase mismatching, and so resonance coupling between them cannot occur. By monitoring the output power of the SMF, as shown in Figs. 4(e) and 4(f), the interference is destructive at 1100 nm and constructive at 1111 nm. At 1350 nm, the LP_{01} modes in the center and suspended cores are phase matched and hence resonance coupling between the two modes occurs. From Figs. 4(d) and (g), it can be observed that all the energy of the LP_{01} mode in the suspended core is completely coupled into the center core, after 16.2 mm of transmission along the HADCF, but the LP_{11} mode is still propagating in the suspended core. Therefore, one resonance dip will appear in the transmission spectrum. In the experimental process, it cannot be guaranteed that the LP_{01} and the LP_{11} modes are excited equally, so the contrast of the interference spectrum may be low. The sensitivities of coupling resonance dip and the interference dips due to salinity and temperature are different, so the simultaneous measurement of salinity and temperature can be realized by monitoring the wavelength drift of both, different types of dips and then solving the coefficient matrix.

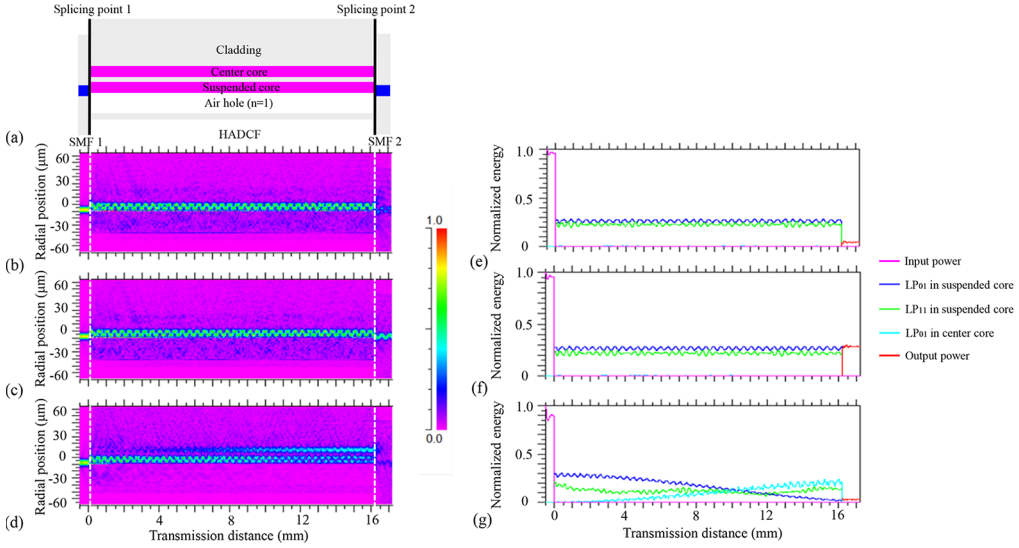

Fig. 4. (a) The schematic diagram of the proposed sensor. (b) to (d) Beam propagation in the HADCF at (b) 1100 nm, (c) 1111 nm, and (d) 1350 nm. (e) to (g) The energy of each mode in the HADCF at (e) 1100 nm, (f) 1111 nm, and (g) 1350 nm.

Optics EXPRESS

3. Fabrication and experimental results

The proposed sensor was fabricated experimentally and investigated. First, the centers of SMF and HADCF were aligned to be co-axial by using the fusion splicer (Fujikura FSM-100P+), as shown in Fig. 5(a). Subsequently, the suspended core of the HADCF was rotated to the y-axis in Fig. 5(b). The SMF was moved 19.2 μm along the + y direction, as shown in Fig. 5(c). Thus, the distance between the centers of the suspended core of HADCF and the core of SMF was 4.2 μm. Then, the SMF and HADCF were fused, as shown in Fig. 5(d). The detailed fusion parameters were as follows: the pre-melting power is 105 bit, the pre-melting time is 30 ms, the main discharge power is 128 bit and the main discharge time is 2980 ms. Second, as shown in Fig. 5(e), the HADCF was cleaved off by a fiber cutting system built in our lab, where the length L of HADCF is 16.2 mm. The cutting length error can be kept within 5 μm. Third, the other side of HADCF was fused with another SMF in the same way mentioned previously, as shown in Fig. 5(f). When two cores were phase matched and placed very close together, the light from one core will be coupled into the other core. The suspended and the center cores of the HADCF could form a directional coupler. In addition, the offset in the fusion between the core of SMF and the suspended core of HADCF can be used to excite simultaneously the LP_{01} mode and LP_{11} mode in the suspended core, to form an MZI based on two-mode interference. To ensure that only the LP_{01} mode and LP_{11} mode in the suspended core of the HADCF are excited, the SMF was offset toward the air hole. Two micropores near the fusion points were prepared by femtosecond laser micromachining to form the microfluidic channel, as shown in Fig. 5(g). Laser ablation was carried out using a Yb:KGW femtosecond laser (Light Conversion PH-2) operating at a wavelength of 1030 nm. The output light was frequency doubled to 515 nm, using a second-harmonic generation module. The laser had a pulse width of 290 fs and a repetition rate of 5 kHz. A low-NA objective (Olympus, NA = 0.25) was used as the focusing lens. A precise three-dimensional displacement stage (Aerotech ABL1000WB, ABL1000, and ANT130V-5) was used to adjust the fiber position in the ablation process. The single-pulse energy of the laser was set to 2 μJ and the laser ablation was completed, layer-by-layer, by using a precision displacement stage and an optical shutter at a speed of 0.1 mm/s. The stage was moved up by 5 μm in the z direction after completing each layer of the ablation process.

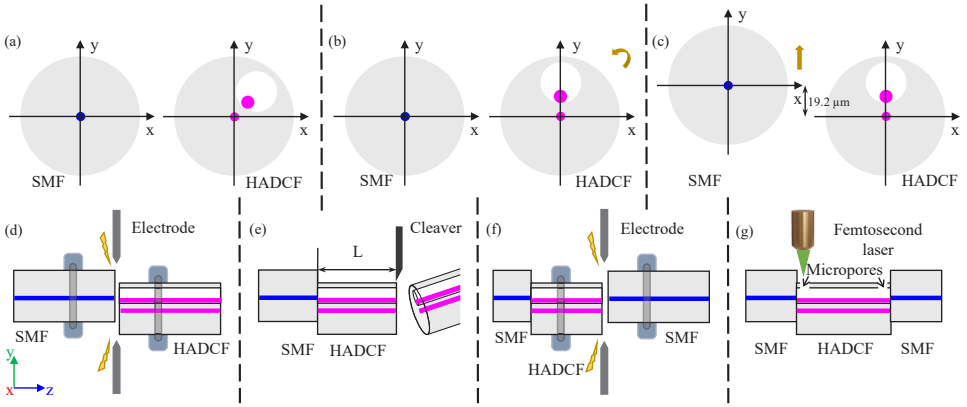

Fig. 5. Schematic diagram of sensor fabrication process.

Figure 6 illustrates the measurement system for detecting the characteristics of the salinity. A super-continuous spectrum laser (NKT Superk COMPACT) was used as the light source, where the transmission spectrum was monitored by using an optical spectrum analyzer (OSA, Yokogawa AQ6370C). One micropore was covered by a syringe needle, and the gap between the syringe

Optics EXPRESS

needle and microslide was sealed with UV glue allowing fluid to be injected into the air hole through the syringe needle. Solutions with different salinities were prepared by mixing NaCl and deionized water ($n = 1.333$) in different ratios.

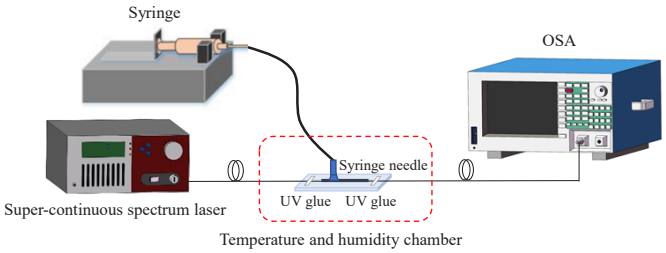

Fig. 6. Schematic diagram of the measurement system for detecting salinity characteristics.

Figures 7(a) and 7(b) show the transmission spectra of the sensor before and after filling with liquid. Their spatial frequency spectra were shown in Figs. 7(c) and 7(d), respectively. Before filling with liquid, the multiple interference dips caused by LP_{01} and LP_{11} modes in the suspended core were observed in the wavelength range of 1100 -1300 nm. In the wavelength range of 1300 - 1400 nm, an obvious resonance coupling dip is seen, overlapping with the interference spectrum. Interference dips disappear when the LP_{11} mode in the suspended core cuts off beyond a wavelength of ~1410 nm. The Peak 1 in Fig. 7(c) can be attributed to the resonance coupling between LP_{01} modes in the center and suspended core. While the Peak 2 can be attributed to the interference between LP_{01} and LP_{11} modes in the suspended core, as the reciprocal of the spatial frequency (ξ_1) of the Peak 2 is equal to the FSR of the transmission spectrum shown in Fig. 7(a) [32]. Other weak peaks in the spatial frequency spectrum are produced by the excited higher-order cladding modes in the HADCF. When the air hole is filled with the liquid, the phase matching wavelength can be seen to show a red shift, as illustrated in Fig. 1(c). Therefore, after filling with distilled water, the resonance coupling dip was seen to be red shifted to a wavelength of 1462.86 nm. Meanwhile, the interference between the LP_{01} and the LP_{11} modes in the suspended core occurs over the wavelength range of 1100 - 1440 nm. The resonance coupling dip is superimposed on the weak interference dips, beyond a wavelength of ~1440 nm. This can be explained in that the LP_{11} mode in the suspended core cuts off near 1440 nm (as shown in Fig. 1(c)), but this has not disappeared completely due to the short HADCF used.

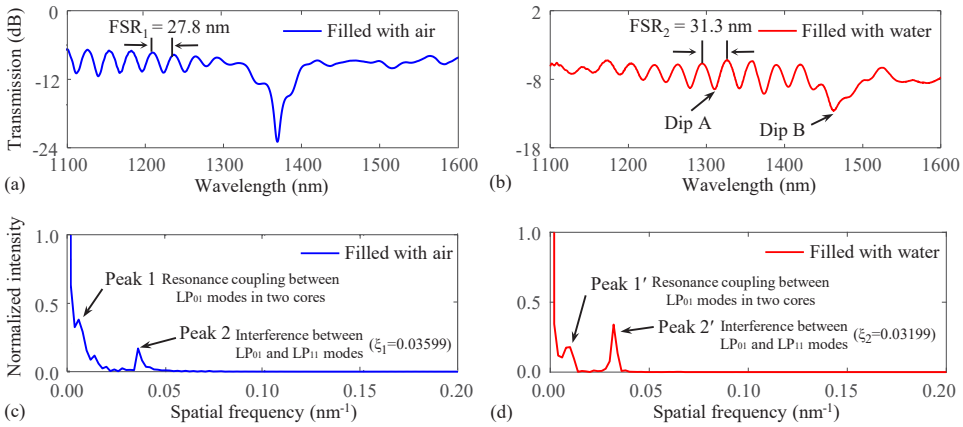

Fig. 7. Transmission spectra and spatial frequency spectra of sample. (a), (c) without liquid and (b), (d) filled with liquid.

Optics EXPRESS

An interference dip (denoted as Dip A) and the resonance coupling dip (denoted as Dip B) were selected to measure the performance of the sensor. The responses of the sensor to salinity at the temperature of 25 °C are shown in Fig. 8, where the salinity range is from 0 to 80 ‰ with a step of 10 ‰. In the experiment, after the saline solution was injured into the air hole through the syringe needle, the sensor was placed in the sink that was full of the solution to be measured. Then the sink was placed into a temperature and humidity chamber and the temperature was set to 25 °C. A thermistor-based thermometer was placed in this sink to measure the temperature of solution. When the temperature of the solution was stabilized at 25 °C, the spectra were recorded. The wavelength of the interference dip was seen to be linearly red-shifted, with the increase of the salinity, while the coupling resonance dip wavelength also shifts to the long wavelength region. The coupling resonance will weaken, since the coupling efficiency between the center core and the suspended core decreases with the increase of the external RI. The sensitivities to salinity of Dip A and Dip B were 135.7 pm/‰ and 190.7 pm/‰, respectively. In addition, the temperature responses were also measured for different salinities, and the result are shown in Fig. 9. (a). The sensor was placed in a temperature and humidity chamber, and the temperature was increased from 0 to 35 °C with a step of 5 °C. When the salinity of the NaCl solution is 80 ‰, the temperature sensitivities of Dip A and Dip B were -74.8 pm/°C and -188.2 pm/°C, respectively. The measured results verify the temperature sensitivities are almost identical for different salinities. Meanwhile, to measure the stability of the sensor, the sensor was placed in the sink filled with the 80 ‰ saline solution after the 80 ‰ saline solution was injured into the air hole of the fiber. The sink was placed into a temperature and humidity chamber and the temperature was set to 25 °C. The humidity was set to 90% to prevent the evaporation of solutions. The recorded wavelengths of dip A and dip B were shown in Fig. 9. (b). The proposed sensor is stable and the drift of the wavelengths of dips is within 0.02 nm in 5 hours. The minor changes of dip A and dip B is caused by the temperature fluctuations in the temperature and humidity chamber.

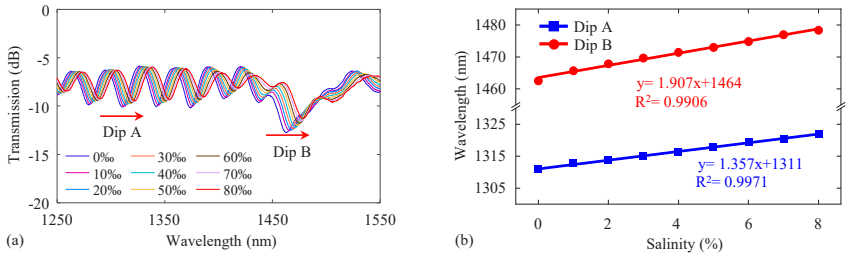

Fig. 8. (a) Transmission spectra of the sensor for different values of salinity. (b) The wavelengths of Dip A and the Dip B as a function of salinity.

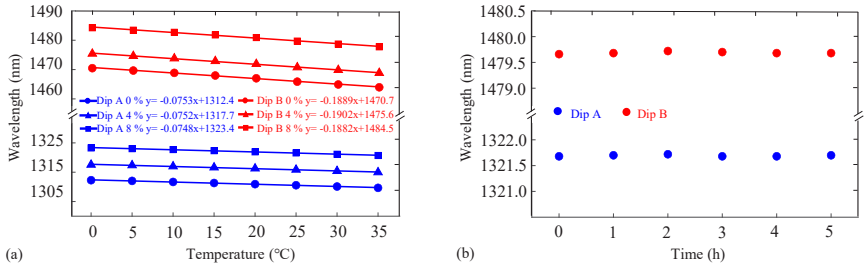

Fig. 9. (a) The wavelengths of Dip A and Dip B as a function of temperature for different salinities. (b) The stability of the sensor.

Optics EXPRESS

Based on the above measurement, a sensitivity matrix could be established as follows:

$$\begin{pmatrix} \Delta\lambda_A \\ \Delta\lambda_B \end{pmatrix} = \begin{pmatrix} 135.7\text{pm}/‰ & -74.8\ \text{pm}/^\circ\text{C} \\ 190.7\text{pm}/‰ & -188.2\ \text{pm}/^\circ\text{C} \end{pmatrix} \times \begin{pmatrix} \Delta S \\ \Delta T \end{pmatrix} \tag{8}$$

By substituting the experimental results into the matrix equation, the changes of salinity and temperature could be obtained at the same time as follows:

$$\begin{pmatrix} \Delta S \\ \Delta T \end{pmatrix} = \begin{pmatrix} 135.7 & -74.8 \\ 190.7 & -188.2 \end{pmatrix}^{-1} \begin{pmatrix} \Delta\lambda_A \\ \Delta\lambda_B \end{pmatrix} \tag{9}$$

In order to make an analysis of the error induced by the sensitivity matrix, the following measurement was operated. The reference salinity S_{ref} and temperature T_{ref} are set to be 80 ‰ and 25 °C, respectively. The measured wavelength of dip A and dip B are 1321.58 nm and 1479.70 nm. Four-group measurements are completed to get $\Delta\lambda_A$ and $\Delta\lambda_B$ relative to the initial condition. After that, the variation of the salinity (ΔS_{mea}) and temperature (ΔT_{mea}) were obtained by Eq. (9). The results are shown in Table 1. The maximum detection errors for the salinity and temperature are 1.61 ‰ and 0.50 °C. It can be explained that the salinity sensitivity is slightly different at each temperature (compared to reference condition: 25 °C) and the temperature sensitivity is slightly different at each salinity (compared to reference condition: 80 ‰).

The performance comparison between the proposed sensor and other reported sensors is shown in Table 2. Compared with some reported sensors [6,7,18,34,35], the proposed dual-parameter sensor has a higher salinity sensitivity, which is attributed to the strong interaction between light and solution due to the direct contact between the suspended core and the liquid solution. In addition, an MZI and a directional coupler are constructed parallelly in a single HADCF.

Table 1. Simultaneous detection of salinity and temperature

ΔS_{set} (‰)	ΔT_{set} (°C)	$\Delta\lambda_A$ (nm)	$\Delta\lambda_B$ (nm)	ΔS_{mea} (‰)	ΔT_{mea} (°C)
0	5	-0.46	-1.02	-0.91	4.50
-40	0	-5.44	-7.68	-39.86	0.42
-40	10	-6.38	-9.78	-41.61	9.80
-80	5	-11.46	-16.90	-79.18	9.60

Table 2. Comparison of sensing performance of different salinity sensors

Structure	Salinity sensitivity (pm/‰)	Temperature sensitivity (pm/°C)	Size of sensor (mm)	Reference
Long-period fiber grating (LPFG)	125.5	-	50	[6]
Multimode interference	19.4	-	59	[35]
Two-core fiber coupler	205.9	-	50	[15]
Long-period grating (LPG) based MZI	6.61	53	73.8	[34]
Etched fiber Bragg grating (FBG)	11.09; 90.66	31.2; 43.5	20	[7]
Photonic crystal fiber Sagnac interference with FBG	12.68; 0	-14.9; 10.6	208	[18]
Microfiber Mach-Zehnder interferometer (MMZI)	482; 1075	-516; -856	40	[33]
HADCF coupler with MZI	135.7; 190.7	-74.8; -188.2	16.2	This work

Optics EXPRESS

Compared with some dual-parameter sensors [7,18,33,34], the proposed sensor has a smaller size and higher integration.

4. Conclusion

In conclusion, an optical fiber sensor based on a HADCF and used for the simultaneous measurement of temperature and salinity has been experimentally demonstrated. A section of HADCF was fused between two SMFs with an optimized offset. The HADCF can be regarded as a composite structure, composed of an MZI and a directional coupler. Based on the unique HADCF, the MZI and directional coupler are integrated parallelly, which guarantee a high salinity sensitivity and a small size of the sensor. At the phase mismatching wavelength, interference occurs between the LP_{01} and the LP_{11} modes in the suspended core. Near the phase matching wavelength, resonance coupling occurs between the LP_{01} modes in the center and the suspended cores. The two-mode interferometer and the directional coupler have different sensitivities to salinity and temperature. The sensitivities to salinity and to temperature of the interference dip were 135.7 pm/‰ and -74.8 pm/°C, respectively. The sensitivities to salinity and temperature of the coupling dip at longer wavelengths are 190.7 pm/‰ and -188.2 pm/°C, respectively. The sensor discussed has the advantages of simplicity in the fabrication, offering a high integration and facility for dual parameter measurement, making it a promising candidate for sensing in the marine environmental field.

Funding. National Natural Science Foundation of China (62105077, 62175049, 62275061); Natural Science Foundation of Heilongjiang Province (YQ2021F002); Fundamental Research Funds for the Central Universities (3072022CF2505, 3072022TS2501).

Disclosures. The authors declare no conflicts of interest.

Data availability. Data underlying the results presented in this paper are not publicly available at this time but may be obtained from the authors upon reasonable request.

References

1. J. Cullum, D. P. Stevens, and M. M. Joshi, "Importance of ocean salinity for climate and habitability," Proc. Natl. Acad. Sci. U. S. A. **113**(16), 4278–4283 (2016).
2. H. Denkilkian, A. Koulakezian, R. Ohannessian, M. S. Chalfoun, M. Joujou, A. Chehab, and I. H. Elhajj, "Wireless sensor for continuous real-time oil spill thickness and location measurement," IEEE Trans. Instrum. Meas. **58**(12), 4001–4011 (2009).
3. L. Cao, Y. Yu, M. Xiao, J. Yang, X. Zhang, and Z. Meng, "High sensitivity conductivity-temperature-depth sensing based on an optical microfiber coupler combined fiber loop," Chin. Opt. Lett. **18**(1), 011202 (2020).
4. Y. P. Liao, J. Wang, H. J. Yang, X. Wang, and S. Wang, "Salinity sensing based on microfiber knot resonator," Sens. Actuators, A **233**, 22–25 (2015).
5. H. Z. Yang, X. G. Qiao, K. S. Lim, S. W. Harun, W. Y. Chong, M. R. Islam, and H. Ahmad, "Optical fiber sensing of salinity and liquid level," IEEE Photonics Technol. Lett. **26**(17), 1742–1745 (2014).
6. F. Yang, R. Hlushko, D. Wu, S. A. Sukhishvili, H. Du, and F. Tian, "Ocean salinity sensing using long-period fiber gratings functionalized with layer-by-layer hydrogels," ACS Omega **4**(1), 2134–2141 (2019).
7. D. Luo, J. Ma, Z. Ibrahim, and Z. Ismail, "Etched FBG coated with polyimide for simultaneous detection the salinity and temperature," Opt. Commun. **392**, 218–222 (2017).
8. Z. T. Lin, R. Q. Lv, Y. Zhao, and H. K. Zheng, "High-sensitivity salinity measurement sensor based on no-core fiber," Sens. Actuators, A **305**, 111947 (2020).
9. R. Flores, R. Janeiro, and J. Viegas, "Optical fibre Fabry-Perot interferometer based on inline microcavities for salinity and temperature sensing," Sci. Rep. **9**(1), 9556 (2019).
10. Y. Zhao, Q. L. Wu, and Y. N. Zhang, "Simultaneous measurement of salinity, temperature and pressure in seawater using optical fiber SPR sensor," Measurement **148**, 106792 (2019).
11. X. C. Yang, Z. Wang, Y. H. Liu, and J. Q. Yao, "SPR sensor based on exposed core micro-structured optical fiber for salinity detection with temperature self-compensation," Opt. Mater. Express **11**(8), 2468–2477 (2021).
12. Y. Zhao, Q. L. Wu, and Y. N. Zhang, "Theoretical analysis of high-sensitive seawater temperature and salinity measurement based on C-type micro-structured fiber," Sens. Actuators, B **258**, 822–828 (2018).
13. H. A. Rahman, S. W. Harun, M. Yasin, S. W. Phang, S. S. A. Damanhuri, H. Arof, and H. Ahmad, "Tapered plastic multimode fiber sensor for salinity detection," Sens. Actuators, A **171**(2), 219–222 (2011).

Optics EXPRESS

14. Z. Zhou, Z. Gong, B. Dong, S. Ruan, and C. C. Chan, "Enhanced sensitivity refractometer based on spherical Mach-Zehnder interferometer with side-polished structure," IEEE Sens. J. **21**(2), 1548–1553 (2021).
15. J. R. Guzman-Sepulveda, V. I. Ruiz-Perez, M. Torres-Cisneros, J. J. Sanchez-Mondragon, and D. A. May-Arrioja, "Fiber optic sensor for high-sensitivity salinity measurement," IEEE Photonics Technol. Lett. **25**(23), 2323–2326 (2013).
16. L. Wu, J. Guo, Q. Wang, S. Lu, X. Dai, Y. Xiang, and D. Fan, "Sensitivity enhancement by using few-layer black phosphorus-graphene/TMDCs heterostructure in surface plasmon resonance biochemical sensor," Sens. Actuators, B **249**, 542–548 (2017).
17. M. Hernaez, B. Acevedo, A. G. Mayes, and S. Melendi-Espina, "High-performance optical fiber humidity sensor based on lossy mode resonance using a nanostructured polyethylenimine and graphene oxide coating," Sens. Actuators, B **286**, 408–414 (2019).
18. C. Wu, B. O. Guan, C. Lu, and H. Y. Tam, "Salinity sensor based on polyimide-coated photonic crystal fiber," Opt. Express **19**(21), 20003–20008 (2011).
19. M. Hernaez, A. G. Mayes, and S. Melendi-Espina, "Graphene Oxide in lossy mode resonance-based optical fiber sensors for ethanol detection," Sensors **18**(2), 58 (2017).
20. D. Yi, C. Wang, L. Gao, Y. Chen, F. Liu, Y. Geng, H. Zhang, and X. Li, "Ti_3CN MXene-based ultra-sensitive optical fiber salinity sensor," Opt. Lett. **47**(1), 138–141 (2022).
21. R. Pan, W. Yang, L. Li, Y. Yang, X. Yu, J. Fan, S. Yu, Y. Xiong, and L. Zhang, "All-fiber Fabry-Perot interferometer gas refractive index sensor based on hole-assisted one-core fiber and vernier effect," IEEE Sens. J. **21**(14), 15417–15424 (2021).
22. J. A. Flores-Bravo, M. A. Illarramendi, J. Zubia, and J. Villatoro, "Optical fiber interferometer for temperature-independent refractive index measuring over a broad range," Opt. Laser Technol. **139**, 106977 (2021).
23. T. Liu, J. Wang, Y. Liao, X. Wang, and S. Wang, "All-fiber Mach-Zehnder interferometer for tunable two quasi-continuous points' temperature sensing in seawater," Opt. Express **26**(9), 12277–12290 (2018).
24. Y. Liao, J. Wang, S. Wang, H. Yang, and X. Wang, "Simultaneous measurement of seawater temperature and salinity based on microfiber MZ interferometer with a knot resonator," J. Lightwave Technol. **34**(23), 5378–5384 (2016).
25. L. Zhang, D. N. Wang, J. Liu, and H. F. Chen, "Simultaneous refractive index and temperature sensing with precise sensing location," IEEE Photonics Technol. Lett. **28**(8), 891–894 (2016).
26. N. Xie, H. Zhang, B. Liu, H. Liu, T. Liu, and C. Wang, "In-line microfiber-assisted Mach-Zehnder interferometer for microfluidic highly sensitive measurement of salinity," IEEE Sens. J. **18**(21), 8767–8772 (2018).
27. Z. T. Lin, Y. Zhao, R. Q. Lv, H. K. Zheng, and Q. Zhao, "High-sensitivity salinity sensor based on etched C-type micro-structured fiber sensing structure," Sens. Actuators, A **339**, 113518 (2022).
28. H. Zheng, R. Lv, Y. Zhao, R. Tong, Z. Lin, X. Wang, Y. Zhou, and Q. Zhao, "Multifunctional optical fiber sensor for simultaneous measurement of temperature and salinity," Opt. Lett. **45**(24), 6631–6634 (2020).
29. F. Ahmed, V. Ahsani, A. Saad, and M. B. G. Jun, "Bragg Grating embedded in Mach-Zehnder interferometer for refractive index and temperature sensing," IEEE Photonics Technol. Lett. **28**(18), 1968–1971 (2016).
30. X. Yu, X. Chen, D. Bu, J. Zhang, and S. Liu, "In-fiber modal interferometer for simultaneous measurement of refractive index and temperature," IEEE Photonics Technol. Lett. **28**(2), 189–192 (2016).
31. B. Sun, F. Fang, Z. Zhang, J. Xu, and L. Zhang, "High-sensitivity and low-temperature magnetic field sensor based on tapered two-mode fiber interference," Opt. Lett. **43**(6), 1311–1314 (2018).
32. H. Y. Choi, M. J. Kim, and B. H. Lee, "All-fiber Mach-Zehnder type interferometers formed in photonic crystal fiber," Opt. Express **15**(9), 5711–5780 (2007).
33. L. H. Zhang, J. Wang, J. C. Liu, J. C. Zhang, Y. F. Hou, and S. S. Wang, "Encapsulation research of microfiber Mach-Zehnder interferometer temperature and salinity sensor in seawater," IEEE Sens. J. **21**(20), 22803–22813 (2021).
34. G. R. C. Possetti, R. C. Kamikawachi, C. L. Prevedello, M. Muller, and J. L. Fabris, "Salinity measurement in water environment with a long period grating based interferometer," Meas. Sci. Technol. **20**(3), 034003 (2009).
35. Q. Meng, X. Dong, K. Ni, and Y. Li, "Optical fiber laser salinity sensor based on multimode interference effect," IEEE Sens. J. **14**(6), 1813–1816 (2014).